Design of a Biomimetic Controlled-Curvature Robotic Pectoral Fin

John Palmisano, Ravi Ramamurti, Kerr-Jia Lu, Jonah Cohen, William Sandberg, and Banahalli Ratna

***Abstract*—This paper describes the design, construction, and testing of a biomimetic pectoral (side) fin with actively controlled curvature for UUV propulsion. First, a 3D unsteady computational fluid dynamics (CFD) analysis tool has been adapted to computationally optimize any fin design, followed by a full parametric study based on our findings. Second, this said fin has been constructed, and our working optimized mechanical design is offered. Lastly, we make an experimental vs. computational result comparison for thrust, lift, and flapping moment data – showing that a UUV with this technology can have dramatic improvements in low-speed propulsion and control over traditional thruster methods.**

Index Terms – biomimetic pectoral fin, CFD, UUV, adaptive curvature, compliant mechanism

I. Introduction

THE unmanned underwater vehicle, or UUV, has proven to be very useful and effective for a plethora of marine-based applications including hull inspection, military surveillance, underwater mine detection, and exploration. Today's UUV technology excels at several main difficult tasks – long distance traversal (such as with gliders), extreme depth diving, and high speed straight-line motion. However, current UUV technology has performance deficiencies in confined, shallow water scenarios where currents can change unpredictably and where low speed maneuverability within complex near shoreline environments is required. Considering that many UUV applications concern near-shoreline operations, to have a system capable of operating in such unpredictable environments is highly advantageous.

Conventionally, a UUV employs ducted propellers for locomotion. But despite this technology being a proven standard, a great multitude of these thrusters are needed to maintain low speed controllability in all 6 degrees of freedom. This traditional rotating thruster also has the serious problem of getting tangled in near shoreline vegetation. On the contrary, nature has a different approach – fish commonly use their pectoral fins as the primary control mechanism for stability in unpredictable flow fields. As such, imitating this ability can dramatically improve low-speed UUV propulsion and control.

To study the pectoral fin in isolation, as the subject of our analysis we chose the species *Gomphosus varius* (bird wrasse, Fig. 1). What makes this labrid type fish unique is that it uses the pectoral fin as its only locomotive actuator, allowing us to disregard body undulation and the effects of all other fins commonly found on fish.

Fig. 1 Bird wrasse (*Gomphosus Varius*)

The pectoral fin is a very complex propulsor, with many shape-changing intricacies. What we have found is that an actively controlled deforming fin curvature, especially the leading-edge curvature as identified in the bird wrasse, contributes significantly to propulsive ability. To ignore the importance of a controlled fin curvature will only result in designs with reduced operational performance. Yet in the literature [1], no flapping pectoral fin with an actively controlled, quantitatively specified curvature time-history has been reported. Therefore we present our novel working design of a biomimetic pectoral fin propulsor with actively controlled curvature.

This study begins with an in-depth analysis of the common bird wrasse pectoral fin, placing emphasis on fin kinematics [2][3], fluid dynamics [3], and anatomy [2][4]. After simulating these three main variables using CFD, we studied the effects of modifying each to gain an understanding of the various parameters. A parametric study will be given to aid in future pectoral fin design. We will then present the design and rationale of the physically constructed device that can produce the required fin kinematics. Lastly, the fin will be used to experimentally verify the CFD results and determine power requirements.

II. Parametric Study Using CFD

To understand the effects of fin kinematics on propulsive force production, we used a 3D unsteady computational fluid dynamics code, FEFLO (Fig. 2), which is an unstructured grid-based unsteady Navier-Stokes solver with automatic adaptive remeshing [5]. Already successfully demonstrated [6][7][8][9], this computational capability was extremely important in designing the pectoral fin. Not only did it help us rule out ineffective designs such as a rigid flapping fin [10][11], but also in testing design variations in search for performance gains.

Manuscript received January 31, 2007. This work was supported in part by Office of Naval Research.

K. Lu is with the Department of Mechanical and Aerospace Engineering, George Washington University, Washington, DC (e-mail: kjlu@gwu.edu).

All other authors are with the Naval Research Laboratory in Washington, DC (e-mail: banahalli.ratna@cbmse.nrl.navy.mil, palmisano@gmail.com).

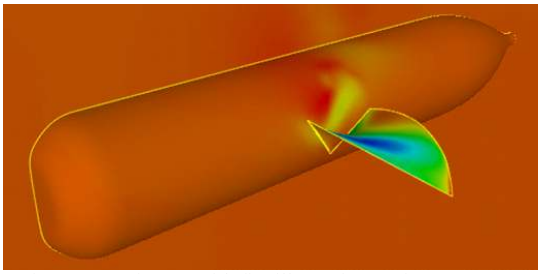

Fig. 2 CFD of UUV with fin, illustrating surface curvature
Colors represent the magnitude of hydrodynamic pressure.

In this manner, we identified five major independent parameters that can be varied to change the force generation time-history during a stroke cycle. Presented is our rationale for choosing the specified values for each parameter.

A. Fin Surface Curvature

The fin surface curvature is defined as the shape of the fin with respect to time. Recreating this curvature was the most complex part of the design. There are 14 fin rays (also referred to as ribs) in the bird wrasse pectoral fin (Fig. 3), each contributing to the fin curvature kinematics. For simplicity of design, manufacture, actuation, and control, it is ideal to have the fewest possible number of ribs. But for more effective fin propulsion, it is ideal to maximize the number of ribs – more control points result in a smoother fit to desired fin curvature time-histories. Using CFD it was determined that 5 ribs (Fig. 4.) resulted in a good balance between effective curvature and our specific mechanical implementation constraints [10].

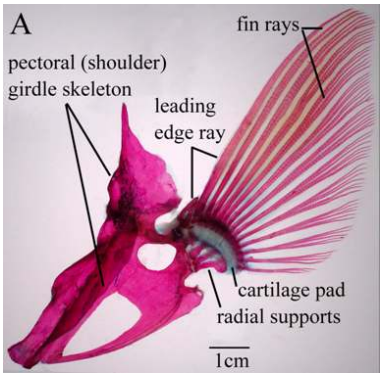

Fig. 3 Anatomy of bird wrasse fin [4]

The pectoral fin of the bird wrasse also exhibits what is called splaying, similar to spreading apart the fingers of a hand. Although the CFD results showed that this additional degree of freedom to incorporate splay resulted in greater propulsion, we decided this improvement was not significant enough to warrant the additional mechanical and control complexity. Our analysis determined that ribs moving independently in parallel planes offered effective thrust.

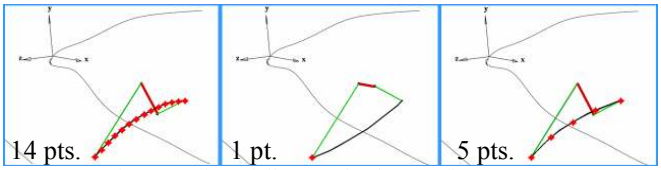

Fig. 4 Number of rib control points vs. fin curvature
5 control points balance simplicity with a smooth curve fit.

The overall rib and fin dimensions (Fig. 5) are scaled up bird wrasse pectoral fin measurements. This scaling was done so as to match our operational UUV requirements, while minor dimensional changes were made to factor in our mechanical simplifications. Since CFD results show smaller rib spacing will result in higher propulsive thrust [10], we set it to our devices' minimum mechanically possible value of .8 cm. This gives the fin an aspect ratio (AR, the square of the leading edge length divided by the projected area of the fin) near 4.5. This is consistent with the morphology of common labrid fish, as fast fish tend to have an AR closer to 5 while slow fish have an AR closer to 1 [12].

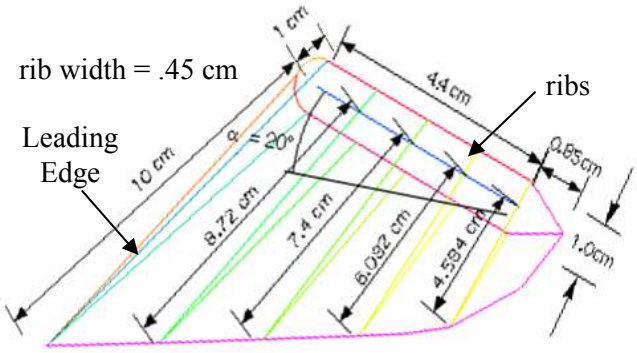

Fig. 5 Pectoral fin rib design with measurements

By imitating observed bird wrasse kinematics [2], we have determined an effective fin tip deflection time profile to define fin curvature. Fig. 6 represents the tip deflection time-history through one stroke cycle, where tip deflection is defined as the angle of a line drawn from the tip of the rib to the axis of rotation with respect to the neutral position. The actual curvature of the rib is defined by rib geometry and changes as a function of tip deflection. Due to a small deflection angle, rib 3 will only passively actuate between ribs 2 and 4.

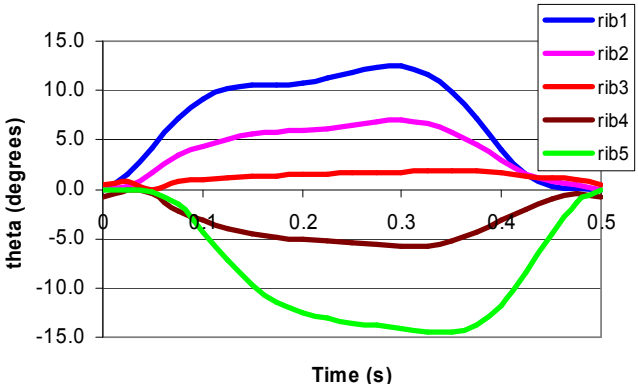

Fig. 6 Individual rib tip deflection angle vs. time (at 2 Hz) kinematics
Kinematics are based on simplified kinematics of the bird wrasse.

B. *Angle of Attack*

The angle of attack, α, is the angle of the fin root with respect to the horizontal axis (Fig. 5, Fig. 7). In the bird wrasse pectoral fin, this angle varies throughout the stroke cycle. However, a CFD analysis based on our simplified design and specific curvature time-history showed no thrust benefit to varying α over time. Instead, a fixed α of 20° was found to maximize forward thrust. Again, this is consistent with the morphology of common labrid fish, as fast fish tend to have an α closer to 20° while slow fish have an α closer to 70° [12]. Because experimental data was collected in still water, α is fixed at 0° in order to minimize complexity. A simple mathematical rotation can be performed to determine thrust and lift at an α of 20°.

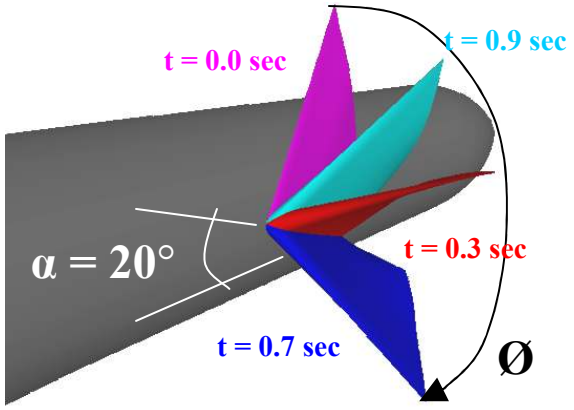

Fig. 7 α, Ø, and fin curvature vs. time (at 1 Hz)

C. *Bulk Rotation Angle*

The bulk rotation angle, Ø, is the peak-to-peak amplitude of a stroke (Fig. 7). In the bird wrasse, this angle is about 74°. However, we found that as the bulk rotation angle increases, the thrust will also increase. We chose a nominal peak-to-peak amplitude of 114° for our design, but this angle can be increased or decreased in flight by a controller for various operational conditions. Fig. 7 shows the fin in several positions during a full stroke while Fig. 8 specifies the angle with respect to time. Total rib tip motion is the sum of the rib angles in Fig. 6 and the bulk angle in Fig. 8. Note that an increase in bulk rotation angle results in an increase of sinusoidal lift amplitude – an effect potentially degrading to vehicle stability.

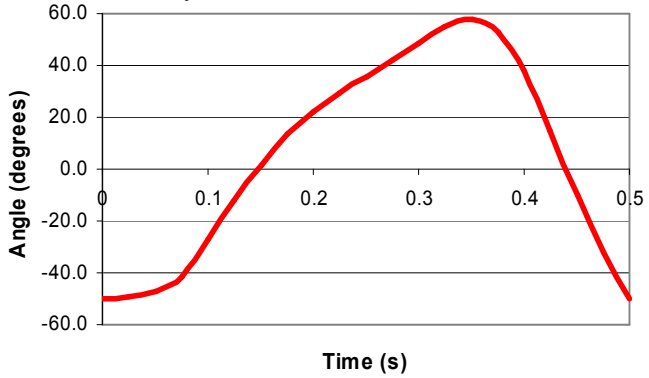

Fig. 8 The specified bulk rotation angle vs. time (at 2 Hz)

D. *Frequency*

Frequency is the number of cycles per second at which the fin oscillates. In CFD, the frequency was varied between 0.3Hz and 3.3Hz to study its effects on propulsion. It has been found that the upstroke thrust production increases as the square of the frequency ratio [10]. A frequency of 1.2 Hz was chosen as a compromise between effective fin operation and mechanical limitations. Similar to varying the bulk rotation angle, changing the frequency can also be used as a vehicle control parameter.

E. *Velocity*

The last parameter is the nominal forward velocity at which a fin-based vehicle would be required to travel at. CFD studies have been performed for vehicle velocities from 0 knots to 3 knots at flapping frequencies of 1 Hz to 2 Hz. The analysis showed that a vehicle is capable of sustaining a 2 knot velocity while maintaining position with a fin flapping frequency of 2 Hz and bulk rotation angle of 114° [10].

III. Construction

Using the CFD results, and inspiration from the biological construction of the bird wrasse, we proceeded to construct the device. When encountering implementation conflicts, it was common to refer back to CFD to understand how a modification would affect propulsion.

There are four main construction issues to address. The first is to design an actively deforming rib that we can exert full control over. The second is to make a flexible skin connecting the ribs to serve as the fin surface area. The third is to select small, lightweight, feedback controllable actuators that can independently bend each rib. The last issue is to devise a method for bulk rotation actuation.

A. *Flexible Ribs*

Our fin design starts with the structural analysis, optimization, and construction of each of the five artificial ribs. A cross sectional view of a bird wrasse fin ray is schematically shown in Fig. 9. Interestingly, although entirely unintentional and purely a product of optimization, our design is very similar to how nature builds and actuates the pectoral fin rib.

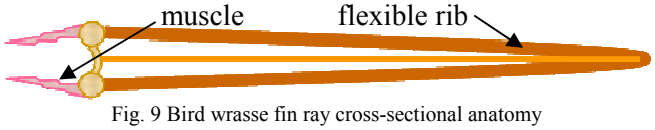

Fig. 9 Bird wrasse fin ray cross-sectional anatomy

Our fin rib is a compliant structure, designed to bend at specific base-to-tip deflection angles (Fig. 6) when subjected to translational forces at the base (Fig. 10a). The fin is composed of five of these independent ribs, and when actuated in particular patterns, their independent deflections are combined to create fin curvature such as in Fig. 11.

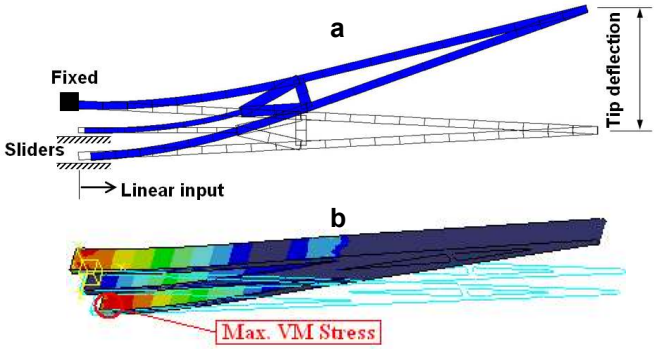

Fig. 10 (a) Rib bending curvature and tip deflection analysis
(b) Rib FEA analysis to design for rib damage prevention

To build the artificial ribs, the structural material used should have as high S/E ratio as possible (where S is strength and E is Young's modulus) [13] to allow flexing without failure. The topology of the compliant ribs was designed by using a structural-optimization based synthesis approach (Fig. 10a) [14] and FEA (Fig. 10b).

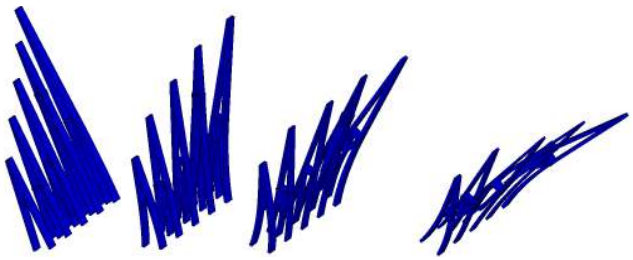

Fig. 11 Independently bending ribs forming pectoral fin curvature

The objective of this rib optimization problem was to ensure the ribs could achieve the required deflection under fluid pressure when subjected to linear actuation at the base. At the same time, the actuation force and resulting stresses must be kept within material property limits and actuator capabilities. As a worst case scenario, because the fluid pressure varies throughout the fin stroke, we used the CFD computed pressure distribution at the instance when the fluid creates the maximum moment about the bulk rotation axis.

Ease of manufacturing was a major requirement for rib optimization. A large variety of manufacturing methods and materials have been attempted for the ribs, including several 3D printers and multiple hand-made methods. In addition, we experimented with different rib materials including bronze, several steels, carbon fiber, ABS, and various other plastics. The most viable option identified, based on requirements and manufacturability, was 3D printing using ABS. The five designed ribs, each individually optimized based on different required lengths and curvatures, were built from ABS as shown in Fig. 12. Each rib is actuated at the mechanical interface, with push rods actuating the ribs at the pin joints linearly along the slider interface. Well placed cross beams help significantly in preventing fluid pressure from buckling the ribs. A rounded leading edge on the first rib was subjectively added with the intention of reducing fluid drag. Each rib was experimentally tested in water over 10^4 cycles without material failure, and individual rib force from FEA (Fig. 10b) was experimentally verified using a force sensor.

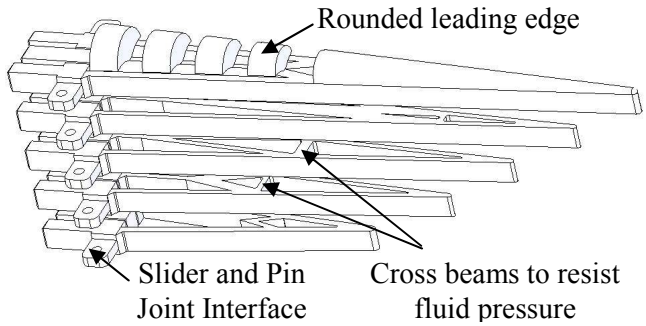

Fig. 12 Set of five artificial ribs made from an ABS 3D printer
Each rib shape is individually optimized based on length and curvature.

B. *Flexible Skin*

A flexible skin is added to create a surface area between the individual ribs (Fig. 13). This skin must easily stretch under rib deflection, yet not sag under fluid pressure. To produce such a skin, we used Smooth-On's Dragon Skin Silicon Rubber™ de-gassed under vacuum, and cured into large thin flexible sheets. These sheets are then cut to size, wrapped around the fin, and glued to each rib with Sil-Poxy™ silicon rubber adhesive. The Young's Modulus of this skin is 240kPa; the tensile strength is 3.3MPa; the Poisson's ratio is .35; and it has verified elongation of 1000% before failure. The skin was tested for chemical stability in sea water with no detectable degradation over a one month period. Skin thickness optimization was done experimentally and verified through FEA. Thick skin was shown to contribute significantly to required input force, while skin made too thin would tear. Our chosen fin skin thickness measures .4mm ± .1mm. The empty space inside the fin is allowed to fill with water in order to equalize hydraulic pressure and reduce skin sagging. For easier filming and analysis of rib movement, the skin material was also selected for its translucent properties.

Fig. 13 Fin without and with flexible skin

C. *Rib Actuation and Feedback Control*

Futaba S31100 hobby servos are used as feedback controllable rib actuators (Fig. 14). Control in this manner is straightforward, simple to implement, and very affordable. All parts were made from ABS by 3D printing.

All servos are controlled by the PIC16F877 microcontroller with a read-through list of pre-defined rotation angles and timing data points. Seven selected points for each of the four actuated ribs are used during a complete

stroke cycle. These servo rotation angles are determined by manually measuring servo angle vs. rib curvature (Fig. 6) for each individual rib. The same microcontroller simultaneously collects all sensory data. Because this 20MHz microcontroller still has a considerable number of unused clock-cycles remaining, this demonstrates that only minimal computational processing power is required to control this pectoral fin.

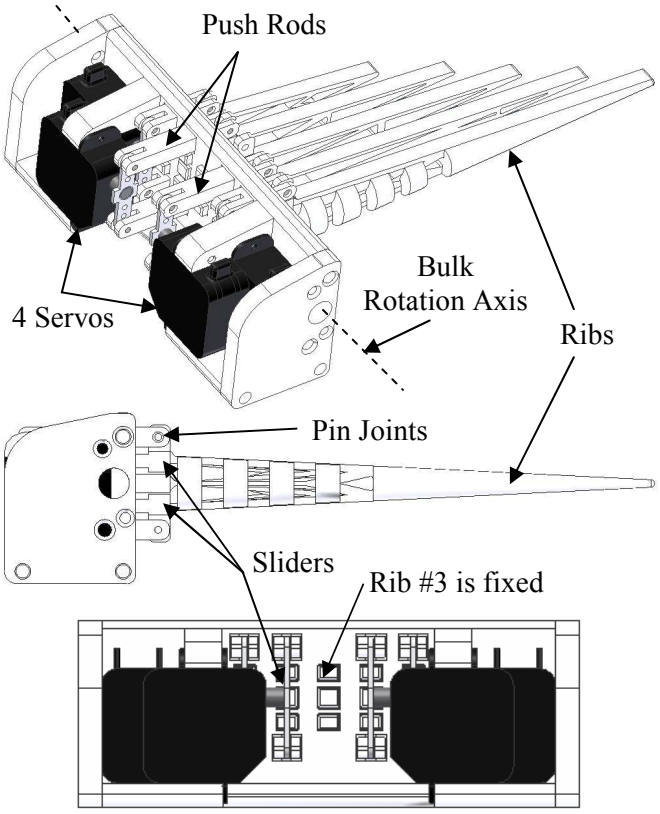

Fig. 14 Isometric, frontal, and top design views of fin system
Servos push the 'push rods' to controllably bend the ribs

D. Bulk Rotation (Fin Flapping)

The bulk rotation time-history (Fig. 8) is also controlled through a set of 7 data points. The design uses a Hitec HSR-5995 hobby servo motor (Fig. 15, Fig. 16) to produce the required bulk rotational torque (.2 Nm at peak) and rotation angle about the bulk rotation axis (Fig. 14, Fig. 16). The mechanical response rate of this bulk rotation servo is the limiting factor for oscillation frequency.

IV. Test Setup And Results

Fig. 15 and Fig. 16 show the test setup used to evaluate the performance of our fin design. Fin kinematics, generated forces, and power are measured. All following measured data are for still water at a bulk rotation angle of 114°, an angle of attack of 0°, and a cycle frequency of 1.2 Hz.

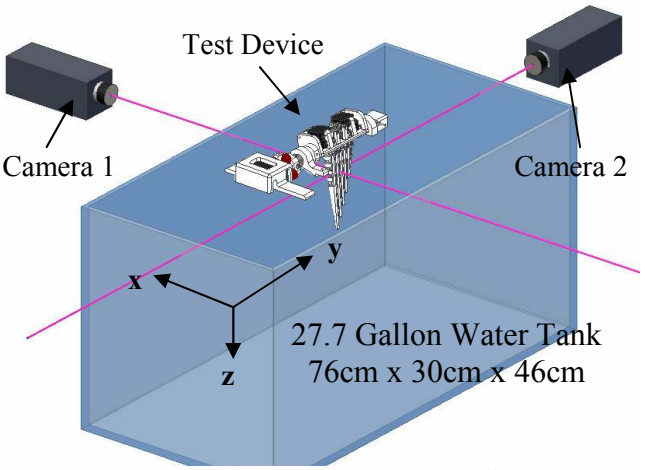

Fig. 15 Test setup: high speed camera setup, sensor/fin locations

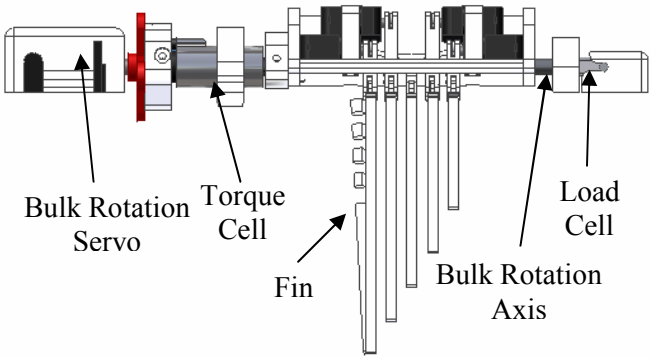

Fig. 16 Test device close-up: sensor locations, side view of fin

A. Kinematics Measurements

The fin's flexible ribs may deviate from the designed deflection angle due to fluid-structure interaction. To verify that the specified kinematics (Fig. 6) matched the actual experimental kinematics, we traced the 3D location of each rib tip across an entire cycle. Two high speed digital video cameras (Fig. 15), angled at 90° to each other, synchronously recorded images of the flapping fin at a predefined time step. Using image analysis software [15], matching rib tip coordinates selected from these image sequences were transformed into 3D coordinates (Fig. 17).

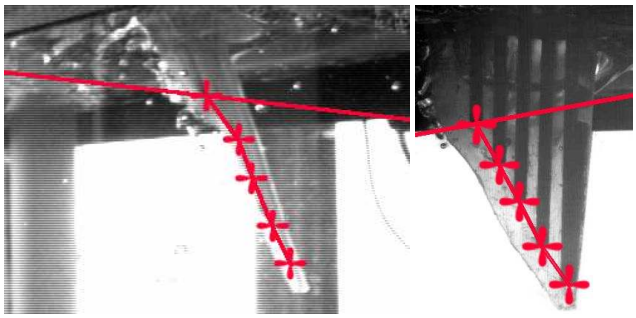

Fig. 17 Matching 2D points to determine 3D kinematics of rib tips

This analysis software calculates the intersecting fields of view by implementation of a transformation matrix created using the direct linear transformation method. To ensure that the transformation matrix is not optically distorted, a

calibration is made using an object that covers the fields of view of both cameras and has known global 3D coordinates. By locating the rib tips in this coordinate system, kinematics can then be calculated accurately. Fig. 18 is a side by side comparison of desired rib tip + bulk rotation angles vs. actual experimental data.

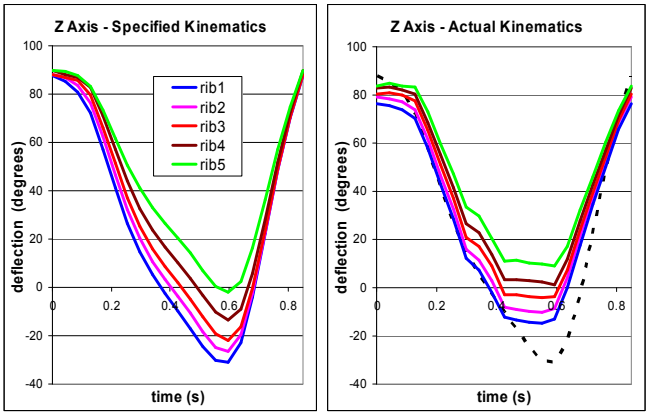

Fig. 18 Left: Specified CFD rib tip angle + bulk rotation angle (1.2Hz); Right: Actual experimental camera measurements (1.2Hz)

Fluid-structure interaction is not accounted for in the CFD analysis. The fluid forces calculated are determined based on the user specified rib tip deflections, yet these deflections can only be determined correctly when the fluid forces are known. Therefore, to show rib design a success, a comparison of kinematics are made with (in water) and without (in air) these fluid forces and shown in Fig. 19. Because there is only a minor tip deviation, error can be considered small and negligible. If one wishes to correct for this error, the servo control system can be reprogrammed to over-deflect each rib thereby balancing out this unwanted deviation. However, this tedious iterative correction process was not performed for reasons discussed in section VI.

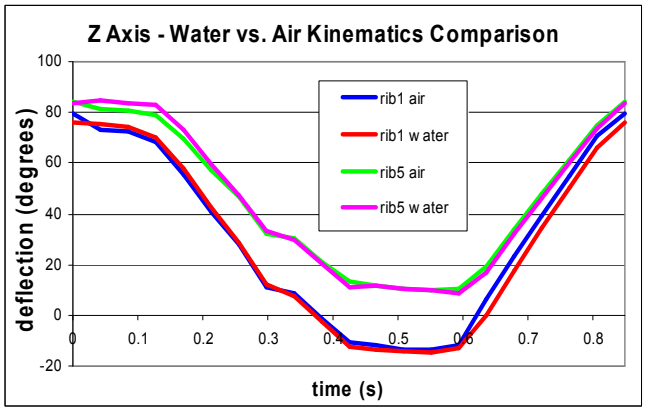

Fig. 19 Rib deflections + bulk rotation kinematics in air and in water

B. *Force Measurements*

We used a torque cell and a load cell (coaxial with the bulk rotation axis) to measure the thrust, lift, and bulk moment (Fig. 14). These forces are resolved into thrust and lift vectors with respect to a notational UUV (Fig. 2). To remove the dynamic effects of the actual mechanical device not present in CFD (rotational inertia, friction, vibration, etc.), experimental measurements were made both in air and in water. At each time step, the in-air results were then subtracted from the in-water results to obtain the true thrust and lift. Minor measurement error is introduced using this method, as the in-air kinematics are not 100% representative of the in-water kinematics (Fig. 19). CFD results for lift, thrust, and moment data are provided as a side-by-side comparison with experimental data (sampling rate of 86 points per cycle) over three complete cycles in Fig. 20.

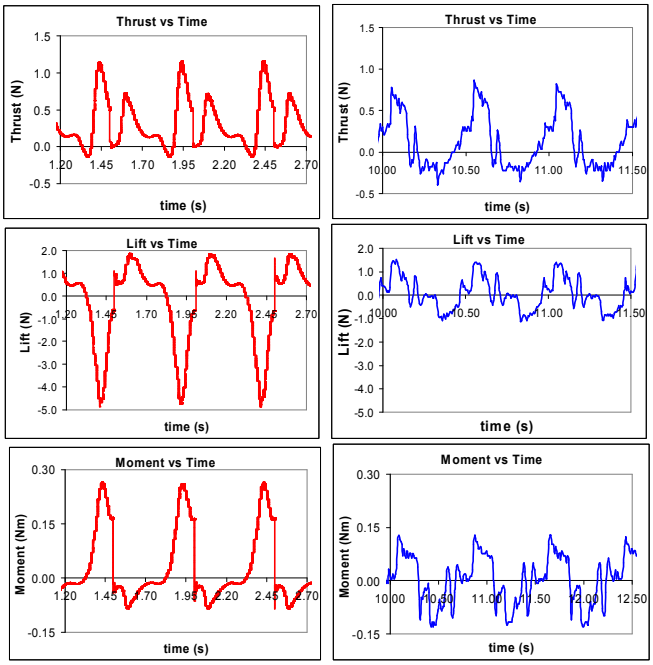

Fig. 20 CFD Fin (left) vs. Experimental Results (right) over 3 cycles

C. *Power Requirements*

Knowing energy consumption and efficiency is important in understanding system performance and electrical requirements. In the experiment, individual power consumption of each servo was obtained real-time by using a current-sense amplifier IC. Average power is shown in Table I, with each servo labeled by the fin component it drives. Rib 1 requires significant power because of its high bending angle and long moment arm. Rib 5 requires the most because of its high bending angle to length ratio, resulting in high internal material bending resistance.

TABLE I
EXPERIMENTALLY DETERMINED MEAN SERVO POWER CONSUMPTION

	Rib 1	Rib 2	Rib 4	Rib 5	Bulk	Total
Power (W)	3.16	..36	.38	3.39	2.52	9.81

Total power consumption at steady state for each actuator is graphed over time in Fig. 21. Control electronics, such as the microcontroller and sensors, consumed an additional 0.3W. A notional two-fin UUV, with a 6V NiMH battery rated at 4 Ah, would have a continuous runtime of 1.2 hours.

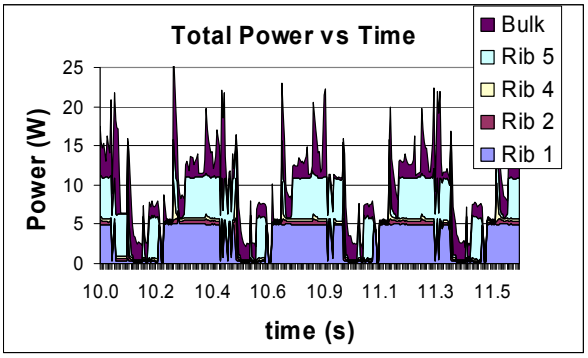

Fig. 21 Power Consumption vs. Time, at steady state

Both Fig. 21 and Table I give realistic and practical power consumption data for the fin design. For comparison, a power analysis was also done using CFD. This result ignores the additional energy required to flex the skin, to drive inefficient actuators, to counter mechanical friction and rotational inertia, and to resist internal bending stresses of each rib. Instead, this datum is based on determining the absolute minimum required energy to use this fin with our specified kinematics and fin dimensions. As calculated by CFD, the mean power required per stroke cycle was found to be .127 W of power.

V. Flow Visualization

To better understand fin-fluid interaction, we observed both experimentally and computationally how fluid flows across the fin during the stroke cycle. Fig. 22 shows in 2D a laminar flow encountering the front of the fin, with a turbulent wake being jettisoned out behind the fin. Shed vortices are seen throughout the wake.

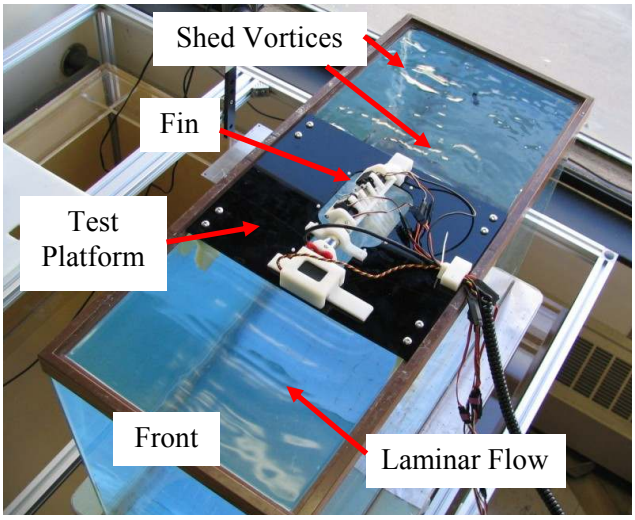

Fig. 22 Experimental setup with 2D surface flow visualization

Two instantaneous snapshots of 3D unsteady flow visualization by CFD particle tracing is shown in Fig. 23. This fluid flow has been confirmed by experimental dye tracing in Fig. 24. Water re-circulates across the bottom of the tank for the return trip to the front.

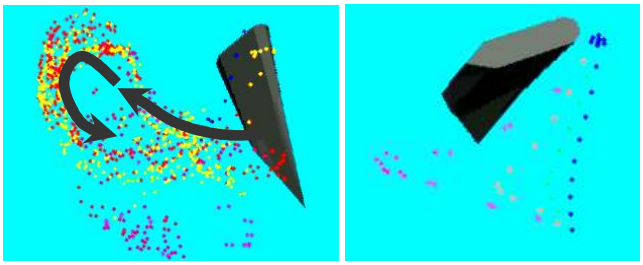

Fig. 23 Left: CFD particle tracing of fluid flow (at 1000 particles)
Right: Top view, showing flow field around fin

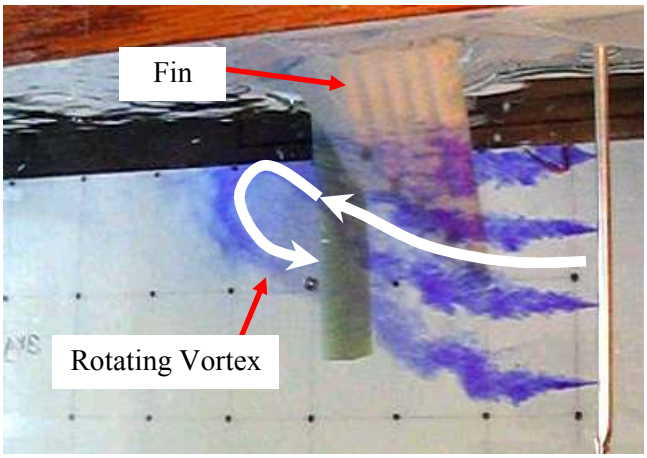

Fig. 24 Experimental dye tracing visualization of fluid flow

VI. Sources of Error And Discussion

Although results are similar and on the same magnitude as computed results (Fig. 20), there are two sources of error that will explain the discrepancy. The first source is due to an unavoidable test setup constraint. In CFD, the fin fluid dynamics is computed by analyzing an entirely submerged fin. However, to protect the expensive load and torque sensors from water damage, our fin rotation axis was located 1.3cm above the water surface. This resulted in undeterminable surface level interactions such as waves and air ingestion that our CFD does not account for. Additionally, unavoidable sensor resolution plus sensor response time error was calculated to be within +/- 5%, while experimental cycle to cycle mean varies +/- 10%.

The second source results from intentionally un-tuned kinematics (Fig. 18). To experimentally produce rib kinematics exactly as defined in the CFD would require an unnecessarily long iterative tweaking process. Instead, our goal is to produce similar kinematics, and then recompute those experimentally measured kinematics in CFD to generate a new computationally determined lift, thrust, and moment data set. This way we can validate the original CFD results, and know that the computed propulsive forces are attainable, given that the kinematics are equal. The similarity between our experimental propulsive forces and those in the recomputed CFD data set (Fig. 25) demonstrates this validation. Because our experimental calibration has not yet been fine tuned, an artificial scaling of moment vs. time data is shown in Fig. 26 for a qualitative comparison.

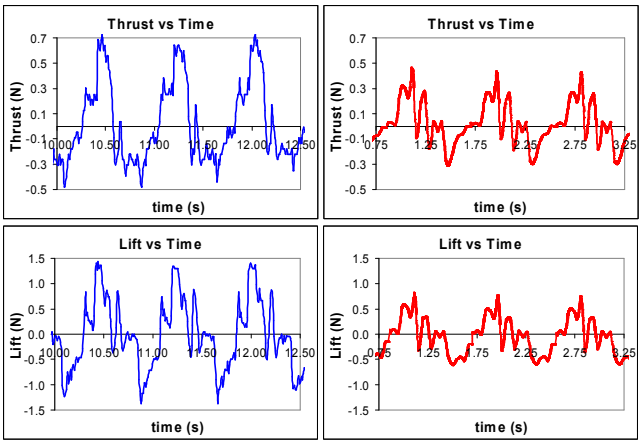

Fig. 25 Left: Experimental results (repeated from Fig. 20)
Right: Recomputed CFD results using experimental kinematics

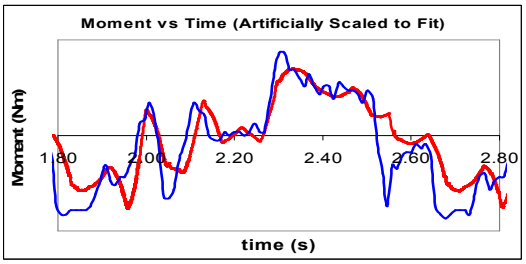

Fig. 26 Moment: Experimental (blue) artificially scaled to fit CFD (red)

A mean comparison, given in Table II, shows the relative match between recomputed CFD results and measured data during steady state. It also shows that actively controlled curvature creates greater thrust than the non-controlled passive curvature. As predicted by CFD analysis and confirmed experimentally, our controlled-curvature pectoral fin design is capable of producing effective propulsion force.

TABLE II
RECOMPUTED CFD VS EXPERIMENTAL PROPULSION COMPARISON

	Recomputed CFD	Experimental (Active Curvature)	Experimental (Passive Curvature)
Thrust	.0262 N	.028 N	.016 N
Lift	-.0289 N	.031 N	.023 N
Moment about α=0°	.0008 Nm	-.0001 Nm	.0000 Nm

VII. FUTURE WORK

After analyzing various boundary dimensions, CFD data showed that the water tank boundary in Fig. 15 significantly affects propulsion (Fig. 25) and energy consumption results (Fig. 21). Therefore these results are not representative of open water infinite boundary conditions. Future work will be done in open water conditions for more applicable data.

The fin has gone through three major design iterations. This current design was optimized in terms of dimensions, power consumption, thrust maximization, and manufacturability for inclusion in a soon to be constructed UUV. We additionally plan to experiment with a range of fin curvature time-histories for better UUV maneuverability.

ACKNOWLEDGMENT

Thanks to Tewodros Mengesha at George Washington University, who gave much support for rapid prototyping the ABS components, Jawad Naciri for help developing the skin, and to Jason Geder, who processed the high speed camera image sequences for conversion from 2D to 3D coordinates. We would also like to acknowledge Prof. Sridhar Kota and Mr. Brian Trease at the University of Michigan for their involvement in initial rib development. And lastly, thanks to Peter Madden of the Lauder Laboratory at Harvard University for providing us his 2D to 3D video analysis software.

REFERENCES

[1] P. Bandyopadhyay, "Trends in Biorobotic Autonomous Undersea Vehicles," *IEEE Journal of Oceanic Engineering*, vol. 30, no. 1, 2005, pp. 109-139.

[2] J. Walker and M. A. Westneat, "Labriform propulsion in fishes: kinematics of flapping aquatic flight in the bird wrasse, Gomphosus varius," *J. Exp. Biol*., vol. 200, 1997, pp. 1549-1569.

[3] R. Ramamurti and W. C. Sandberg, "Fluid dynamics of flapping aquatic flight in the bird wrasse: three-dimensional unsteady computations with fin deformation", *J. Exp. Biol*., vol. 205, 2002, pp. 2997-3008.

[4] M. Westneat, D. Thorsen, and J. Walker, "Structure, Function, and Neural Control of Pectoral Fins in Fishes," *IEEE Journal of Oceanic Engineering*, vol. 29, no. 3, July 2004, pp. 674-683.

[5] R. Löhner, "An adaptive finite element solver for transient problems with moving bodies," Computers and Structures, vol. 30, 1988, pp. 303-317.

[6] R. Ramamurti, R. Löhner, and W. C. Sandberg, "Computation of 3-D Unsteady Flow Past a Tuna with Caudal Fin Oscillation," Advances in Fluid Mechanics, vol. 9, (ed. M. Rahman and C. A. Brebbia), pp. 169-178, Southhampton, UK, Computational Mechanics Publications, 1996.

[7] W. C. Sandberg and R. Ramamurti, "Unsteady Flow Computational Technology for Flapping Fins," Proc. Unmanned Undersea Submersibles Technology Symposium, pp. 182-194, Durham, NH, Autonomous Systems Institute, 1999.

[8] R. Ramamurti, R. Löhner, and W. C. Sandberg, "Computation of the 3-D Unsteady Flow Past Deforming Geometries," Intl. J. Comp. Fluid Dynamics, 13, pp. 83-99, 1999.

[9] R. Ramamurti and W. C. Sandberg, "Simulation of the Flow about Flapping Airfoils Using a Finite-Element Incompressible Flow Solver," AIAA Journal, 39, pp. 253-260, 2001.

[10] R. Ramamurti and W. C. Sandberg, "Computational Fluid Dynamics Study for Optimization of a Fin Design," 24th AIAA Applied Aerodynamics Conference, AIAA-2006-3658, 2006.

[11] R. Ramamurti and W. C. Sandberg, "The influence of fin rigidity and gusts on force production in fishes and insects: a computational study", 42nd AIAA Aerospace Sciences Meeting, AIAA 2004-404, January 2004.

[12] P. Wainwright, D. Bellwood, and M. Westneat, "Ecomorphology of Locomotion in Labrid Fishes," Environmental Biology of Fishes, vol. 65, 2002, pp. 47-62.

[13] L. L Howell, *Compliant Mechanisms*, John Wiley and Sons, Inc., New York, NY, 2001.

[14] B.P. Trease, K.J. Lu, and S. Kota, "Biomimetic Compliant System for Smart Actuator-Driven Aquatic Propulsion: Preliminary Results," ASME Int. Mechanical Eng. Congress & Exposition, Washington, D.C., IMECE2003-41446, 2003.

[15] J. Geder and W. C. Sandberg, "Multi-Camera, High-Speed Imaging System for Flapping Fin Kinematics Measurement," Naval Research Laboratory Memorandum Report NRL/MR 6401-07, submitted for publication January 2007.